

ARTICLE OPEN



Pit-to-crack mechanisms of 316LN stainless steel reinforcement in alkaline solution influenced by strain induced martensite

Ulises Martin^{1,2}, Nick Birbilis³, Digby D. Macdonald⁴ and David M. Bastidas^{1,5}✉

The pit-to-crack transition of AISI 316LN stainless steel reinforcement exposed to stress corrosion cracking (SCC) in chlorides contaminated alkaline environment, was studied by a combination of slow strain rate testing (SSRT) and electrochemical impedance spectroscopy (EIS). The phase angle shift ($\Delta\phi$) obtained by EIS at low frequencies was utilized to determine the pit-to-crack transition, differentiating from crack nucleation and propagation as identified by shifts in the frequency range of phase angle (θ) peaks. The pit-to-crack transition was developed once the maximum θ value shifted from the low to high frequencies. EIS analysis was corroborated by assessment of repassivation rates and pit growth, in addition to calculating $\Delta G^{\gamma-\alpha}$. Crack nucleation at lath martensite developed transgranular SCC. Strain-induced martensitic transformation was associated with the brittle failure of AISI 316LN stainless steel, where α' -martensite phase preferentially incubated the pit, and favored crack nucleation, thus promoting pit-to-crack transition.

npj Materials Degradation (2023)7:88; <https://doi.org/10.1038/s41529-023-00406-w>

INTRODUCTION

Stress corrosion cracking (SCC) occurs in the presence of a corrosive environment and mechanical stimulus, leading to the development of cracks that can propagate and reduce service lifetimes. SCC can develop without significant signs of damage accumulation, and is therefore critical threat for engineering asset management^{1,2}. Austenitic stainless steels, while used in many industries for outstanding corrosion resistance, are not immune to SCC, even under atmospheric conditions and ambient temperatures³. One of the most common causes of SCC for austenitic stainless steel is chloride-induced stress corrosion cracking (Cl⁻-SCC), that develops as transgranular SCC (TG-SCC); which is triggered when a critical chloride threshold is reached in the presence of residual and/or applied loading. Several mechanisms have been proposed to describe Cl⁻-SCC phenomena, including the slip-dissolution model by Newman, where both crack nucleation and propagation are promoted by the dissolution of slip planes, as well as surface film cracking on newly developed fresh planes^{4,5}. Additionally, the cleavage-dissolution model proposes that crack nucleation and propagation stages of SCC are governed by the synergistic effect of brittle rupture of low-surface-energy cleavage planes in conjunction with anodic dissolution⁶.

In marine and coastal environments, where aerosols containing high chloride concentrations are present, environmentally assisted cracking (EAC) develops due to thin-film electrolyte deposition or water droplets⁷⁻⁹. As a result of the higher chloride concentrations, the redox couple Fe²⁺/Fe³⁺ resulting from iron acid hydrolysis locally reduces the pH below 2, enhancing the cathodic hydrogen evolution and promoting hydrogen embrittlement (HE)¹⁰. By concentrated sat droplet experiments under tension, it has been proven that the crack growth was related to hydrogen,

as seen with AISI 304 U-bends stainless steel samples exposed to MgCl₂ droplets at 30 °C and 28% relative humidity^{11,12}. The HE involves the chemisorption of hydrogen at active sites with high stress, like the crack tip and the crack front. The HE mechanisms that better explain this behavior are hydrogen enhanced decohesion (HEDE), adsorption-induced dislocation emission (AIDE), hydrogen-enhanced localized plasticity (HELP), or a combination of some of them due to the complexity of the processes^{13,14}. When hydrogen is present in austenitic stainless steel, the velocity of hydrogen migration through the microstructure was found to be higher than the crack propagation, thus allowing enough time for the hydrogen to diffuse¹⁰. The results of the HE are plastic deformation ahead of the tip of the crack developing the formation of micro-voids (HELP) or, the weakening of interatomic bonds facilitating decohesion (HEDE), both lowering the minimum energy required for the crack advance^{15,16}.

In addition to the EAC aspects playing a role on the SCC mechanisms, austenitic stainless steel can develop microstructural phase transformation during the manufacturing processes or from in-service straining. The strain-induced phase transformation developed solid-state transformation of the austenitic phase (γ -phase) to martensite (either ϵ - and/or α' -phase)¹⁷. The presence of strain-induced martensite lowers the pitting potential and can act as SCC initiation sites, as well as promote crack propagation, thus increasing susceptibility to Cl⁻-SCC¹⁸. The anodic dissolution model of Newman et al.¹⁹ proposed that the crack propagation rate increased when the strain-induced martensite was fractured at grain boundaries ahead of the crack tip. The SCC susceptibility of strain-induced martensite was shown by both electrochemical and optical microscopy characterization in chloride containing solution to lead to a faster crack nucleation, where preferential pitting attack on strongly slip banded austenite and α' -martensite

¹National Center for Education and Research on Corrosion and Materials Performance, NCERCAMP-UA, Corrosion Engineering, The University of Akron, Akron, OH 44325, USA.

²Department of Materials Science and Engineering, Texas A&M University, College Station, TX 77843, USA. ³Faculty of Science, Engineering and the Built Environment, Deakin University, Waurn Ponds, VIC 3216, Australia. ⁴Department of Nuclear Engineering, University of California at Berkeley, Berkeley, CA 94720, USA. ⁵ROSEN USA, 14120 Interdrive East, Houston, TX 77032, USA. ✉email: dbastidas@rosen-group.com

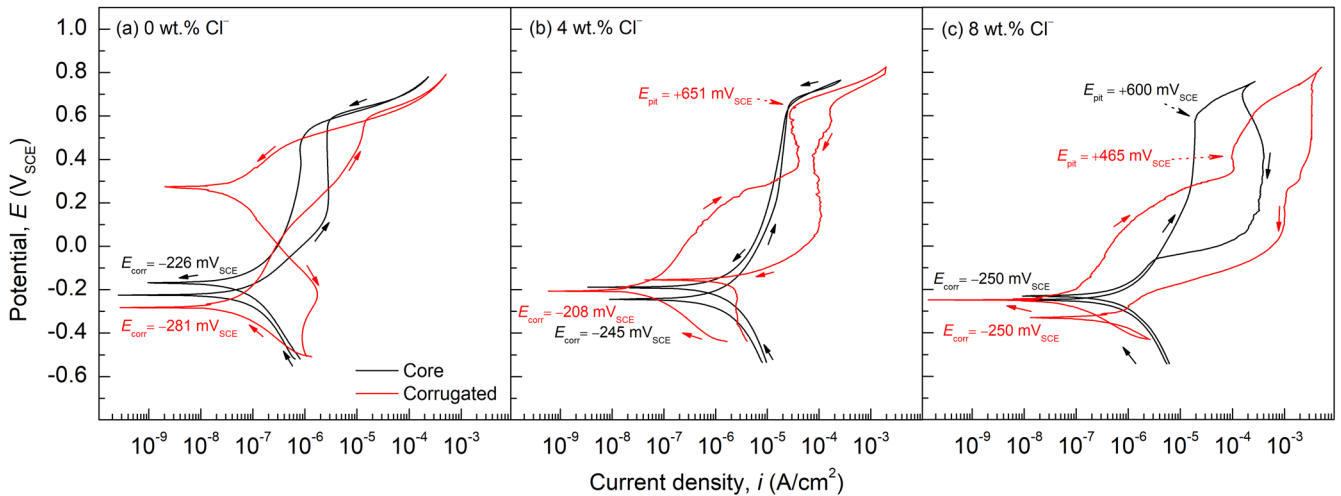


Fig. 1 Cyclic potentiodynamic polarization curves of AISI 316LN SS core and corrugate sections immersed in concrete pore solution. (a) 0 wt.% Cl^- , (b) 4 wt.% Cl^- , and (c) 8 wt.% Cl^- .

Table 1. Electrochemical parameters obtained from the CPP curve for AISI 316LN reinforcement in simulated concrete pore solution at different Cl^- concentrations without any applied stress.

Sample	$[\text{Cl}^-]$	E_{corr} mV _{SCE}	i_{corr} A/cm ²	E_{pit} mV _{SCE}	β_a mV/dec	β_c mV/dec	B mV	PSF
Core	0 wt.%	-226	2.12×10^{-9}	—	276	445	74	—
Corrugated	0 wt.%	-281	1.14×10^{-9}	—	212	245	49	—
Core	4 wt.%	-245	3.67×10^{-7}	—	351	375	79	—
Corrugated	4 wt.%	-208	8.93×10^{-8}	651	325	215	56	0.89
Core	8 wt.%	-250	6.80×10^{-7}	600	485	456	102	0.97
Corrugated	8 wt.%	-250	8.75×10^{-7}	465	314	131	40	1.13

was observed²⁰. The work from Ghosh et al. correlated the effect of strain-induced martensitic transformation to the Cl^- -SCC of AISI 304L at room temperature by U-bend testing²¹. The crack path started at the martensite formed in the outermost surface and followed through the slip bands. Even more, when the alloy had a low stacking fault energy (SFE), the likelihood of promoting strain-induced martensite increased, thus being more prone to suffer from TG-SCC, lowering the chloride concentration threshold to nucleate the first pit²². Alyousif et al. studied the influence of SCC and HE in AISI 304 U-bended stainless steel samples in boiling MgCl_2 solutions, finding that the mechanism responsible for the SCC failure was a combination of strain-induced martensitic transformation and HELP²³. The diffusion of hydrogen atoms ahead of the crack tip promoted a high plastic region, increasing the local stress by an interaction between α' -martensite and the dislocation motion by HELP, prematurely reaching the stress for the crack advance. This was found to be a cyclic process, where the α' -martensite accelerated both the crack nucleation and crack propagation.

However, there is still a lack of knowledge in the effect of strain-induced martensitic transformation in SCC for high alkaline environments, and whether the strain-induced martensitic transformation affects only the rate and path for crack propagation, or if it also accelerates the pit initiation, which eventually would trigger the crack nucleation²⁴. As seen on literature, martensite is more electrochemically active than austenite, becoming the most favorable anodic site, hence initiating the pit nucleation. Furthermore, the high chloride susceptibility of martensite combined with the more brittle phase, can make for a reduction of the minimum pit size for crack nucleation, lowering the stress susceptibility index (K_I) to trigger the pit-to-crack transition²⁵.

In this work, the effect of the strain-induced martensitic transformation on the pit-to-crack transition of AISI 316LN reinforcing stainless steel in alkaline solution containing chlorides was studied using the slow strain rate technique (SSRT). Electrochemical monitoring was also utilized to elucidate the pit-to-crack transition by analysis of current transients and EIS measurements. The crack nucleation and propagation path were correlated with the strain-induced α' -martensite and its influence on the electrochemical SCC mechanism.

RESULTS AND DISCUSSION

Effect of the microstructure and surface on the electrochemical reaction kinetics

Figure 1 shows the cyclic potentiodynamic polarization (CPP) curves for the core and corrugated sections at the three different chloride concentrations. The corresponding corrosion potential (E_{corr}), corrosion current density (i_{corr}), pitting potential (E_{pit}), anodic (β_a) and the cathodic (β_c) Tafel slopes and, the Stern-Geary constant (B) are listed in Table 1. Up to 4 wt.% Cl^- (chloride concentration below the critical chloride threshold of 4.9 wt.% Cl^- for SS in concrete)²⁶, the anodic kinetics for the corrugated samples had similar or lower current densities than the core for electrochemical potentials below the Cr_2O_3 oxidation potential ($\text{Cr}_2\text{O}_3 + 5\text{H}_2\text{O} \rightleftharpoons 2\text{CrO}_4^{2-} + 10\text{H}^+ + 6\text{e}^-$, $E_{\text{Cr}_6/\text{Cr}_3} = +225 \text{ mV}_{\text{SCE}}$ at 12.6 pH)²⁰. However, as the anodic polarization increased, more electrons were supplied, activating the chloride induced pitting mechanism. While the passive oxide film is dissolved due to the higher rate of generation of oxygen vacancies compared to the rate of annihilation of oxygen vacancies supplied by the metal

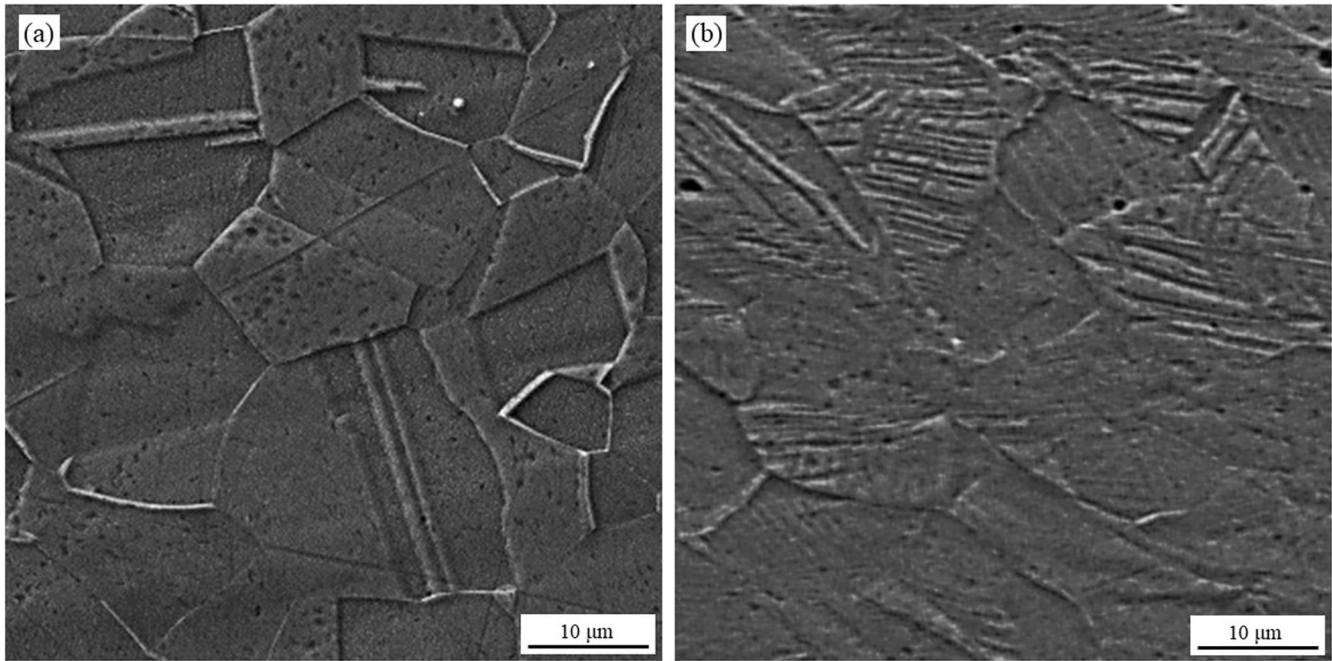


Fig. 2 SEM micrograph of as-received AISI 316LN SS reinforcement. (a) core section 150 \times , and (b) corrugated section 150 \times .

surface, the i raised. At this point, the passive film thinning was triggered until passivity breakdown finally occurred²⁷.

The difference in chloride susceptibility was seen by the development of the E_{pit} at 4 wt.% Cl^- for the corrugate section (+698 mV $_{\text{SCE}}$), while the core sample experienced a negative hysteresis, thus no E_{pit} develops. Furthermore, after the chloride concentration threshold was reached (8 wt.% Cl^-), the core sample developed a E_{pit} at +600 mV $_{\text{SCE}}$, while the corrugated section depicted a E_{pit} value of +465 mV $_{\text{SCE}}$, thus indicating a higher pitting susceptibility of the corrugated section. The β_a values of the core sample revealed a lower electrochemical corrosion kinetics, in addition of the higher B values per chloride concentration of the core than the corrugated samples, indicating a more passive behavior for the core samples. To further compare the dissimilar pitting susceptibility properties between the core and the corrugated sections, the pitting susceptibility factor (PSF) was calculated (see Eq. (1))²⁸:

$$\text{PSF} = \frac{E_{\text{pit}} - E_{\text{rep}}}{E_{\text{pit}} - E_{\text{corr}}} \quad (1)$$

where the PSF is a probabilistic parameter that takes into account the E_{corr} , the E_{pit} , and the repassivation potential (E_{rep}), which is the potential of the backward scan that exhibits a current density of 1 $\mu\text{A}/\text{cm}^2$ ²⁹.

The PSF values below 0.5 indicate low pitting susceptibility, while values equal or greater than 1 indicate high pitting susceptibility. The corrugated sample exposed to 4 and 8 wt.% Cl^- had a PSF of 0.89 and 1.13 respectively, while the core sample only developed a PSF of 0.97 at 8 wt.% Cl^- ; showing the higher pitting susceptibility of the corrugated section compared to the core section.

To evaluate the effect the deformation mechanism had on the electrochemical kinetics, the microstructure of the core and corrugated sections was revealed. Figure 2a shows a γ -phase matrix with some minor deformation twins and slip bands characteristic of face centered cubic (FCC) systems. The corrugated section had a higher density of slip bands, and revealed the development of single and double slip crossover bands within grains (see Fig. 2b). The higher density of planar defects at the corrugated section reduced the mean free path of dislocation

glide, therefore increasing the dislocation pile ups and hindering the corrosion protection properties, which indicates the higher pitting susceptibility of the corrugated section over the core³⁰. The enhanced anodic dissolution kinetics of the corrugated section can be explained by the mechanical energy stored inside the plastically deformed grains, which can be quantified by the residual stress^{31,32}. By performing XRD analysis on the free residual stress peak (found at $2\theta = 147^\circ$ for austenite), a tensile residual stress of 36 ± 12 MPa was obtained, indicating the higher mechanical energy of the surface compared to the core, which had no residual stress. As reported elsewhere, the higher the tensile residual stress the higher the pitting susceptibility, as well as the easier the pit-to-crack transition^{33,34}. In addition, grain refinement was found due to manufacturing process, where the grain size values were 13 ± 2 and 10 ± 3 μm for the core and corrugated sections, respectively.

Effect of the strain-induced martensitic transformation on the pit-to-crack transition

The stress–strain curve including the current transient as a function of the time is presented in Fig. 3a, where the yield strength (σ_y) and the ultimate tensile strength (σ_{UTS}) are labeled with dashed lines^{35,36}. Two regions can be distinguished, resilience from the preload to the σ_y (elastic region, colored in blue) and toughness being from the σ_y to failure (plastic region, colored in green)³⁷. The initial electrochemical current density measurement with an applied stress circa 120 MPa experienced a sharp increase in i starting at 66 $\mu\text{A}/\text{cm}^2$. At this initial loading the nucleation of pits is metastable, as it has not yet reached the E_{pit} (with a corresponding $i = 200$ $\mu\text{A}/\text{cm}^2$). Before the σ_y point (270 MPa), at 192 MPa the recorded i reached the 200 $\mu\text{A}/\text{cm}^2$, which in combination with the induced localized microplastic deformation promoted a stable pit growth³⁸. Once the stress approached the σ_y , the i rose to 430 $\mu\text{A}/\text{cm}^2$, remaining at this value with some minor fluctuations until the σ_{UTS} , where finally the i increased up to the failure. The pit-to-crack transition was calculated by the stress intensity factor to promote SCC (K_{ISCC}), which for stainless steel is around 50 MPa $\sqrt{\text{m}}$ ³⁹. To calculate the K_{ISCC} a hemispherical pit geometry was selected, yielding Eq. (2)⁴⁰:

$$K_{\text{ISCC}} = 1.1215(K_t\sigma)\sqrt{\pi r_{\text{pit}}} \quad (2)$$

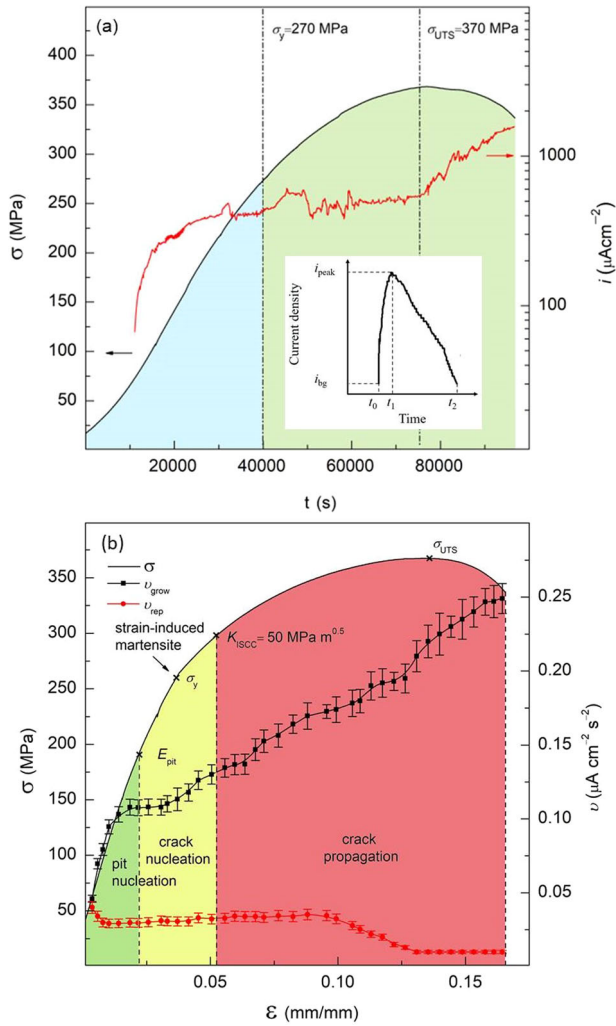


Fig. 3 Stress corrosion cracking testing curves for AISI 316LN SS reinforcement in simulated concrete pore solution with 8 wt.% Cl^- . (a) stress–current transient curves, resilience (blue) and toughness (green), inset showing sketch for the current transient decomposition, and (b) SCC stages with growth (u_{grow}) and repassivation (u_{rep}) rates as a function of strain, showing the different stages for the pit and crack processes, and error bars representing the standard deviation.

where K_t is the stress concentration factor (3 for semicircle), r_{pit} is the radius of the pit, and σ is the normal stress.

The r_{pit} was calculated integrating the monitored current density and converting it to mass loss based on Eq. (3)⁴¹:

$$r_{\text{pit}} = \sqrt[3]{\frac{3EW \int i dt}{2\pi\rho F}} \quad (3)$$

where EW is the equivalent weight, i is the current density, t is the time and ρ is the density.

By assuming the monitored electrochemical current corresponds to the governing anodic dissolution process (i.e., the growth of the dominant pit), the pit-to-crack transition was triggered at 295 MPa (~110% σ_y).

An in-depth analysis of the current transient values shown in Fig. 3a allowed for the pit growth and repassivation rates to be determined (see Fig. 3b). Following the work from Feng et al., each of the current transient peaks can be divided into growth of the pit and its repassivation, where the fitting of each region gives the corresponding rates of growth (u_{grow}) and repassivation (u_{rep}) (Eqs.

(4) and (5))⁴²:

$$u_{\text{grow}} = \frac{i_{\text{peak}} - i_{\text{bg}}}{(t_1 - t_0)^2} \quad (4)$$

$$u_{\text{rep}} = \frac{i_{\text{peak}} - i_{\text{bg}}}{(t_2 - t_1)^2} \quad (5)$$

where t_0 is the start time of the pit, t_1 is the time when maximum peak current occurs, t_2 is the end time of the pit, i_{peak} is the maximum peak current and, i_{bg} is the background current (see Fig. 3a inset).

The u_{grow} always stayed above the u_{rep} during the entire straining, showing that the sample was active for the entire testing and that once the passivity breakdown occurred, no repassivation was possible. From the preload the u_{grow} grew and made a plateau at $0.1 \mu\text{A cm}^{-2} \text{ s}^{-2}$, while the u_{rep} immediately decreased and plateaued around $0.03 \mu\text{A cm}^{-2} \text{ s}^{-2}$. After E_{pit} value is reached, the formation of pits is developed (green region Fig. 3b), where the u_{grow} increased while the u_{rep} remained unchanged. Once the σ_y was reached, the activation of dislocations glide begun, and the strain-induced martensite transformation was triggered. By increasing the density of planar defects, which enhances the α' -phase nucleation, the chloride ions will be easily adsorbed at those anodic sites, thus decreasing the surface energy facilitating the development of the first crack after the K_{ISCC} is reached (crack nucleation stage, yellow region). After the pit-to-crack transition completed, the crack propagation became the governing process and continued until failure (crack propagation stage, red region). For stresses close to the σ_{UTS} , the u_{rep} started decreasing while the u_{grow} kept its increasing trend. This phenomenon is explained by the combination of increased stress and the chloride attack, which make the dissolution and cracking rate to be much greater than the repassivation⁴³. This is in agreement with previous works where due to the increase in dislocation density the dissolution rate increases, depleting the u_{rep} ⁴⁴. After reaching σ_{UTS} the stresses have reached the maximum possible strain-induced martensitic transformation and necking of the sample develops, as observed by the sudden increase of u_{grow} , whereas u_{rep} is almost negligible. The higher anodic dissolution activity than repassivation at the crack tip allows for the crack propagation, which is influenced by the α' -phase strain-induced martensite transformation and the acid hydrolysis of iron at the crack tip⁴⁵.

To further prove the beginning of the strain-induced martensitic transformation at the σ_y , the calculations of the $\Delta G_{\text{total}}^{\gamma \rightarrow \alpha'}$ were made following the work from Patel and Cohen⁴⁶. Assuming that the mechanical stimulus and the chemical thermodynamics governed by the Gibbs free energy are the main factors influencing the transformation, the following formula is obtained (see Eq. (6)):

$$\Delta G_{\text{total}}^{\gamma \rightarrow \alpha'} = -V_m [210.9 - 0.732(M_s + T)] + V_m \left[\frac{\sigma}{2} \times \gamma_0 \times \sin 2\theta + \frac{\sigma}{2} \times \varepsilon_0 \times (1 + \cos 2\theta) \right] \quad (6)$$

where V_m is the molar volume, M_s is the temperature at which the athermal martensite transformation begins, γ_0 is the shear strain, θ is the angle of the applied stress to a potential habit plane normal, and ε_0 is the volume expansion normal to the habit plane⁴⁷.

With M_s being -258°C (calculated based on the elemental composition⁴⁸), T being 25°C , γ_0 being 0.229 and ε_0 being 0.012 both based on variables calculated from the X-ray diffraction (XRD) pattern, V_m being $7.09 \text{ cm}^3/\text{mol}$ for iron and, σ ranging from the σ_y to the σ_{UTS} ⁴⁹. Using Eq. (6), the $\Delta G^{\gamma \rightarrow \alpha'}$ ranged from -2677 to -2738 J/mol . Following the work from Hauser et al., the minimum ΔG value for the strain-induced martensite to form was calculated to be the $\Delta G^{\gamma \rightarrow \alpha'}$ at 0°C , which yielded -2643 J/mol ⁴⁹. Thus, stress values around the σ_y show the strain-induced martensitic transformation is thermodynamically favored, and it is from the σ_y onward that the α' -phase nucleates.

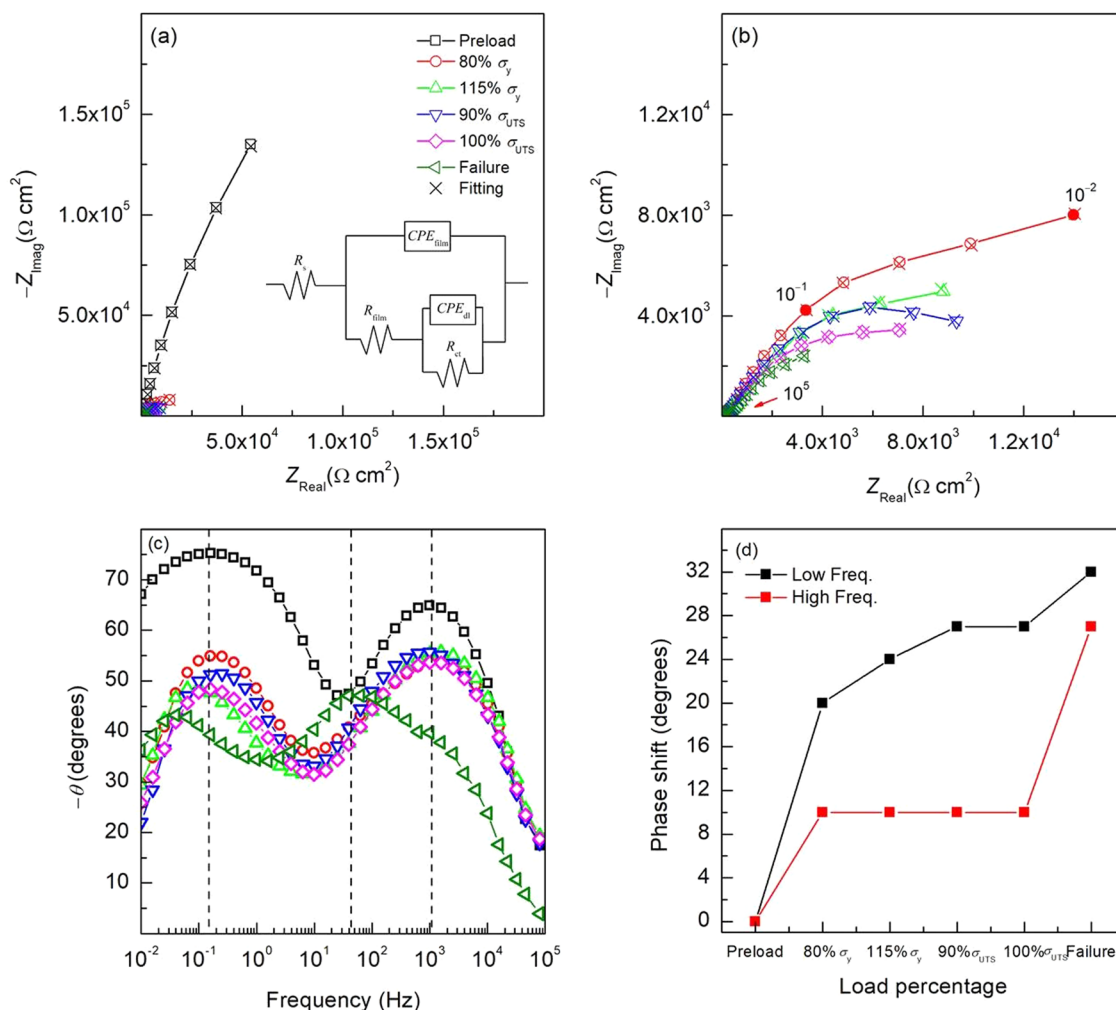


Fig. 4 EIS plots for AISI 316LN SS strained reinforcement in simulated concrete pore solution with 8 wt.% Cl^- . (a) Nyquist diagrams with insert electrical equivalent circuit (EEC) with two time constants, (b) magnification for loading percentages above the preload, (c) Bode plot with the phase angle (θ), and (d) phase shift for low and high frequencies at every load percentage.

Pit-to-crack transition analysis by electrochemical impedance spectroscopy

The EIS results are plotted in the Nyquist diagrams of Fig. 4a, b, where the experimental data was recorded for every percentage of the loading. The Bode plots with the change in the phase angle ($-\theta$) were plotted in Fig. 4c. Before the EIS data was further analyzed, the Kramer-Kronig transforms were performed to show the robustness of the data, proving that there were no artifacts⁵⁰. The electrical equivalent circuit (EEC) used to fit EIS data is shown in the insert of Fig. 4a, having a hierarchically distribution and, being comprised of two times constant in parallel. A good matching was found between EIS fitting data and the experimental values recorded, where the total error was below 10% and chi-squared (χ^2) values in the order of 10^{-4} , proving the goodness of the fitting (see Table 2).

The pseudo-capacitance of the passive oxide film (Y_{film}) progressively increased its value, suggesting a more doped passive film with high density of defects, hence more prone to corrosion – as the pseudo-capacitance values were in the $21\text{--}365 \mu\text{S cm}^{-2} \text{ s}^{n_{\text{film}}}$. The n_{film} values were around 0.7, indicating a rough and defective film due to the n values not reaching the unity⁵¹. The charge transfer resistance (R_{ct}), which accounts for the properties of the electrochemical double layer, started at $108 \text{ k}\Omega \text{ cm}^2$, three orders of magnitude higher than resistance of the film (R_{film})⁵². The high starting values of R_{film} accounted for the developed passive film at the open circuit potential (OCP) prior to

the electrode straining, and as the strain increased in combination with the chloride present in the electrolyte hinders the passive film growth due to the flow of vacancies towards the electrode/electrolyte interface. As the process continued, the higher density of oxygen vacancies doping the passive film promoted the passivity breakdown, as indicated by the lower values of the R_{ct} .

The selection of the CPE over the ideal capacitor was taken upon the non-ideality of the electrochemical interface, first because of the roughness of the corrugated area and also because of the polycrystalline grains forming the microstructure, all having different size and different orientation. As a consequence, the capacitance cannot be directly read as the CPE depicts a branched ladder RC network, therefore, the effective capacitance (C_{eff}) for the passive film and the electrochemical double layer can be obtained (see Eq. (7) for $C_{\text{eff, film}}$ ⁵³ and Eq. (8) for $C_{\text{eff, dl}}$ ⁵⁴):

$$C_{\text{eff, film}} = Y_{\text{film}} (\omega_m'')^{n_{\text{film}} - 1} \quad (7)$$

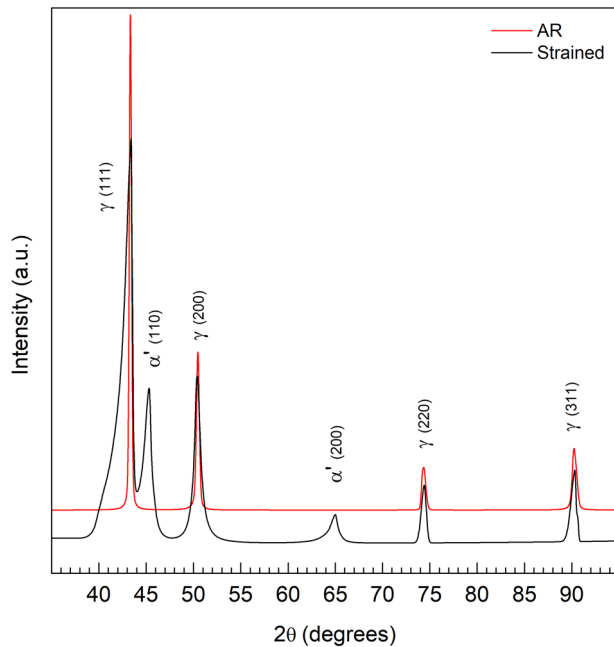
$$C_{\text{eff, dl}} = \left[Y_{\text{dl}} \left(\frac{1}{R_s} + \frac{1}{R_{\text{ct}}} \right)^{(n_{\text{dl}} - 1)} \right]^{\frac{1}{n_{\text{dl}}}} \quad (8)$$

The $C_{\text{eff, film}}$ started at values above the typical $\mu\text{F cm}^{-2}$, which is the order of magnitude expected for a protective passive film, instead it begun at $53 \mu\text{F cm}^{-2}$ and raised up to $2650 \mu\text{F cm}^{-2}$.

Table 2. EIS fitting parameters of AISI 316LN SS reinforcement in simulated concrete pore solution with 8 wt.% Cl⁻, after slow strain rate test (SSRT) at different applied loads.

Applied load	R_s Ω cm	R_{film} Ω cm ²	Y_{film} μS cm ⁻² s ^{n_{film}}	n_{film}	$C_{eff, film}$ μF cm ⁻²	R_{ct} k Ω cm ²	Y_{dl} μS cm ⁻² s ^{n_{dl}}	n_{dl}	$C_{eff, dl}$ μF cm ⁻²	χ^2 (a)
Preload	3	870	21	0.80	53	108	38	0.88	11	1.13×10^{-4}
80% σ_y	3	611	50	0.70	203	24	253	0.76	25	1.26×10^{-4}
115% σ_y	3	465	61	0.69	254	17	308	0.74	26	1.93×10^{-4}
90% σ_{UTS}	3	452	71	0.69	297	13	431	0.72	36	1.75×10^{-4}
100% σ_{UTS}	3	431	77	0.68	337	11	457	0.73	40	2.69×10^{-4}
Failure	3	373	365	0.66	1750	9	932	0.71	86	2.55×10^{-4}

^aError <10% for all values.

**Fig. 5** XRD patterns of AISI 316LN SS reinforcement, as-received (AR) and strained samples.

Such high $C_{eff, film}$ values imply that the passive film is extremely doped with point defects, hence the electron transfer from the electrolyte through the passive film requires less energy. Even more, those $C_{eff, film}$ values, if converted to thickness, would give less than 1 nm, meaning that no passive film is present (as an oxide crystal structure would have a lattice parameter \approx 1 nm). This coincides with the high pitting susceptibility that the corrugated section showed, as well with the high i values recorded during the current transient monitoring. The obtained $C_{eff, dl}$ values show a defective electrochemical double layer, while being between one and two orders of magnitude lower than the $C_{eff, film}$, which had high capacitance values in the order of tenths of $\mu A/cm^2$. The electrochemical double layer, which structure can be explained by Helmholtz model, indicated that the band gap had considerably thinned, almost overlapping the conduction band (E_c) and the valence band (E_v), meaning that the time constant of the passive film was no longer related to a semiconductor but a conductor. This depletion of the space charge is due to the applied potential which raised the OCP above the flatband potential (E_{fb}), forcing the electrons to flow towards the electrolyte.

In addition, EIS data were analyzed to reveal the change of the θ as a function of the frequency was monitored for the different applied stress regions to further elucidate the pit-to-crack

transition, as it has been proven to have a dependency^{55–60}. Figure 4d shows the evolution of the phase angle shift ($\Delta\phi$) as a function of the applied load for the high and low frequencies (taken from Fig. 4c), where the $\Delta\phi$ is the subtraction of the preload to the other applied load points⁶¹. From the preload to the 80% σ_y , the $\Delta\phi$ for both low and high frequencies increased 20 and 10 degrees, respectively; indicating the passivity breakdown developed on similar stress values compared to the ones observed by the current transient monitoring⁵⁶. From that point on, the $\Delta\phi$ of high frequencies did not vary, suggesting that the low frequencies were the responsible for indicating the cracking process; in this case the range was from 0.1 to 1 Hz, in accordance with the literature⁶². The increase of the $\Delta\phi$ after the σ_y for the low frequencies were influenced by the formation of the α' -phase, enhancing the anodic kinetics as also seen from the CPP analysis, but it was not until the maximum value of θ (θ_{max}) shifted from the low frequencies to the high frequencies, that the pit-to-crack transition developed. Similar cracking behavior is seen in literature, where the increase in $\Delta\phi$ denoted the crack nucleation^{57,58}.

The decrease of θ_{max} indicates the crack nucleation and growth, showing the decrease in R_{ct} (as both θ_{max} and R_{ct} are related)⁶³. Furthermore, as the crack incubated, the frequency of the θ_{max} ($f(\theta_{max})$), shifted towards higher frequencies (change from low to high frequencies, see Fig. 4c)⁶¹. The crack propagation was also proof by the $\Delta\phi$ towards lower frequencies of the low frequency peak (both σ_{UTS} points and Failure). Finally, after the increase of the $\Delta\phi$ for low frequencies, the last point before the failure depicted the formation of a third peak at intermediate frequencies (1 Hz), as well as abruptly increasing both low and high $\Delta\phi$. The development of this third relaxation process was due to the large crack propagation and as a consequence, both the θ_{max} and $f(\theta_{max})$ shifted to this third peak (see Failure in Fig. 4c). This third phase angle peak denotes an active cracking process, as explained by Ghobadi et al.⁶⁰.

Effect of the strain-induced martensite on the fracture and crack propagation

Following failure of the AISI 316LN stainless steel reinforcement, XRD was conducted in the as-received (AR) sample as well as in the strained sample (close to the corrugated section) to compare the phase composition (see Fig. 5). The AR sample only had peaks corresponding to the γ -phase, indicating a FCC structure, while the strained sample developed two peaks for the α' -phase having a body centered cubic (BCC) crystal structure⁶⁴. The absent of α' -phase in the AR sample could be due to the overlap of α' -phase (110) with the peak of γ -phase (111) at $2\theta = 43^\circ$ or due to a density of α' -phase below 1 vol.% (limit definition for the equipment). The α' -phase of the strained sample was elucidated and quantified by an approximate value of 13.4 vol.% by the integration of the intensity peaks of each phase⁶⁵. The lattice parameter of the γ - (a_γ) and α' -phase ($a_{\alpha'}$) were calculated,

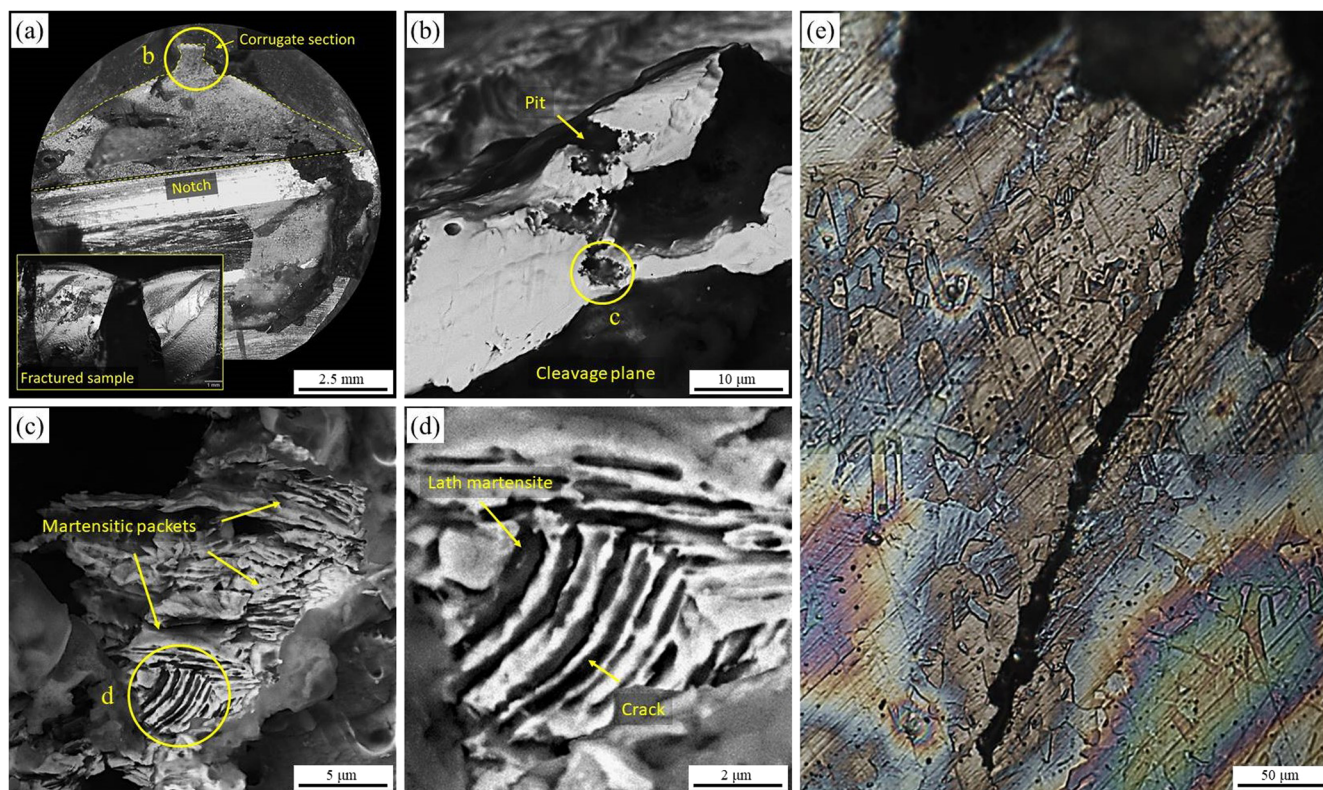


Fig. 6 Surface SEM micrographs of AISI 316LN SS strained reinforcement in simulated concrete pore solution with 8 wt.% Cl^- . (a) fracture plane 100 \times , (b) cleavage plane with martensitic pack inside a pit 1,000 \times , (c) strain-induced martensitic packets 14,000 \times , (d) detail of cracked strain-induced martensitic packet 20,000 \times , and (e) transgranular crack 50 \times .

obtaining a value of 3.575 and 2.849 Å, respectively⁶⁶. As it can be seen the a of the γ -phase is larger than the one from the α' -phase due to the compression stresses that are required for the phase transformation, however the packing factor for the FCC is 74% while for the BCC is only 68%, indicating a higher void volume for the α' -phase⁶⁷. In addition, the calculated tetrahedral void radius of BCC crystal structure was larger than the one from the FCC, being 0.29 r_{Fe} compared with the 0.225 r_{Fe} (r_{Fe} = radius of the Fe atom)⁶⁸. As seen from the work of Zhu, the adsorption of chloride ions on the interstitials minimizes the surface energy of the cleavage planes, thus the α' -phase with its higher void radius will facilitate the formation of cleavage planes (brittle fracture)⁶.

The surface morphology of the fractured sample can be seen in Fig. 6a, where the two sides of the strained sample are shown in the inset. The notch area is delimited by the dotted line, as well as the outer section of the corrugate surface. A brittle fracture mode is shown on the outer section, where the formation of cleavages planes along the corrugate surface are identified (see Fig. 6b). Moreover, those areas presented numerous pits, proving the high chloride susceptibility of the corrugated section. This agrees with the CPP analysis where the corrugated area had a much higher pitting susceptibility, with a PSF > 1 for 8 wt.% Cl^- . In addition, this can be explained by the tensile residual stress obtained from the XRD analysis (36 ± 12 MPa), favoring the pit nucleation, and further crack nucleation³³. The reason of the premature nucleation and fast pit propagation was the strain-induced martensite phase transformation, which acted as a preferential site for the pit nucleation; seen as martensitic packets inside the pits (see Fig. 6c). This more active and brittle martensite α' -phase also enhanced the crack nucleation and propagation, seen by the dissolution of the martensitic packets (gray stripes), while no dissolution was found on the γ -phase matrix (white stripes) (see Fig. 6d). This finding agrees with previous studies of austenitic SS where the

strain-induced martensite enhanced the crack propagation²³. The grain morphology depicted in Fig. 6d resembled an austenitic grain with the formation of lath martensite, where the stripes shape had different directions within the same grain, due to the combination of complex stresses⁶⁹. The cracking of the lath martensite is due to the angular misorientation at the interfaces, this crack propagation is also favored by the anodic dissolution kinetics, thus promoting the SCC mechanism⁷⁰.

Figure 6e indicates a well-defined perpendicular crack to the surface, initiated on the outermost surface where the strain-induced martensite was located (Fig. 6b), propagating towards the inside through the austenite grains following slip bands and further α' -phase (TG-SCC morphology)¹⁸. The transgranular crack was measured by ImageJ software to propagate over 222 μm depth with an average width of 6.84 μm (based on Fig. 6e). This width was smaller than the average grain size of the γ -phase matrix (13 μm), indicating that the dissolution process did not completely dissolve the grains.

The inverse pole figure (IPF) map of the AR (Fig. 7a) and strained samples (Fig. 7d notch and Fig. 7g corrugate) indicates polygonal shape γ -phase grains with some aligned small local misorientation domains, which were attributed to the plastic strain forming dislocation channels where the strain-induced martensite would be promoted (see Fig. 7d, g)⁷¹. These misoriented domains formed specific chain-like formations with different contrast to the parent γ -phase matrix. To verify the nature of the phase transformation, the phase maps were also added, revealing that no hexagonal close-packed ϵ -phase was detected from the Kikuchi pattern analysis. The γ -phase matrix was colored in green, and as it can be seen for the AR sample, no traces of α' -phase (red) were seen (see Fig. 7b). In the case of the strained samples, γ -phase and α' -phase were found, coinciding with the crystallographic analysis from the XRD (see Fig. 7e, h)⁷². The strain-induced

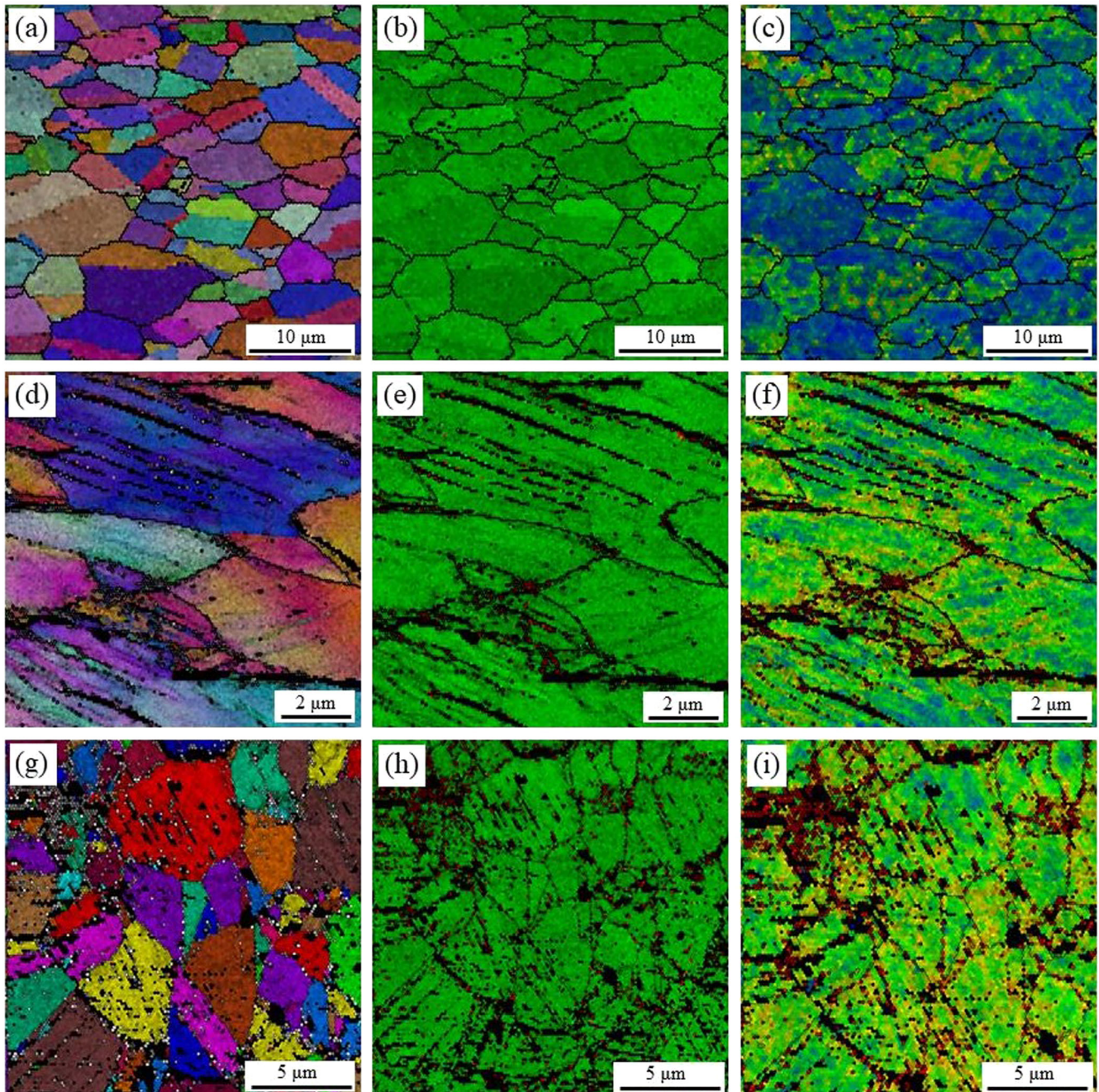


Fig. 7 EBSD analysis of AISI 316LN reinforcement; core area of as-received (AR) sample. (a) Inverse pole figure (IPF) mapping, (b) phase map, and (c) kernel average misorientation (KAM) mapping; notched area of strained sample (d) IPF mapping, (e) phase map, (f) KAM mapping, corrugate area of strained sample (g) IPF mapping, (h) phase map, and (i) KAM mapping.

martensitic transformation commenced at slip bands, and followed a parallel path along such bands, as observed seen in the misoriented domains (Fig. 7d, g)⁷³. Kernel average misorientation (KAM) mapping was carried out to evaluate local changes in alloy structure; whilst for this study KAM was calculated using nearest neighbors with a maximum misorientation of 5°. As observed from Fig. 7c, the majority of the KAM map revealed low to no deformation (green to blue color), with some minor regions of greenish-yellow areas attributed to deformation twins, sites with gathered plastic energy. Nonetheless, for the strained samples, where the slip bands and α' -phase domains were located higher KAM values were found, this is due to the dislocation and planar defects acting as obstacles for dislocation

motion (red color) (Fig. 7f, i). As a conclusion, by combining the higher strains observed on the α' -phase by EBSD with its higher chloride pitting susceptibility seen by the electrochemical testing, it is to expect that SCC mechanism is governed by the α' -phase martensite transformation. Which agrees with previous literature studies where strain-induced martensite was seen to be the main cause for SCC development on austenitic stainless steel⁷⁴.

In summary, the study herein revealed that the SCC mechanisms responsible for the brittle fracture of AISI 316LN stainless steel rebars in alkaline environment was the strain-induced martensitic transformation, where α' -phase preferentially incubated the pit, and promoted the pit-to-crack nucleation. The combination of the higher strains observed on the α' -phase by

EBSD with its higher chloride pitting susceptibility seen by the electrochemical testing, agrees with previous literature studies where strain-induced martensite was seen to be the main cause for SCC development on austenitic stainless steel⁷⁴. It was also proved that stress values around the σ_y made the strain-induced martensitic transformation thermodynamically favored, and it is from the σ_y onward that the α' -phase nucleated.

METHODS

Materials

The material used was AISI 316LN stainless steel rebar grade 75, the elemental composition of which can be seen in Table 3. AISI 316LN reinforcing stainless steel was manufactured by hot-rolling process at a temperature of 890 °C with a post processing of pickling and passivation as per the manufacturer specifications (NAS, North American Stainless). The reinforcing stainless steel specimens were so-called size 3 (3/8 inches, 9.5 mm diameter). The AISI 316LN reinforcement was cut and prepared following ISO 7539-6:2018⁷⁵. To accelerate the crack nucleation process the specimens were machined with a sharp 60° V-notch in the center of the 60 mm corrugated section (see Fig. 8)⁷⁶. Before the samples were attached to the electrochemical cell for the SCC test, they were rinsed with deionized (DI) water, degreased with acetone and blown-dried with air. A 3 cm² exposed area was selected by coating with epoxy lacquer (Midas 335-009 non-conductive paint) (see Fig. 8b).

Slow strain rate testing

Reinforcement steel specimens were subjected to a uniaxial tensile test by slow strain rate testing (SSRT) while being immersed in a corrosive media following the ASTM-G129 standard⁷⁷. The testing solution was simulated concrete pore solution (pH 12.6) made out of a saturated Ca(OH)₂ contaminated with 8 wt.% Cl⁻ by means of CaCl₂ additions. The pH of the electrolyte solution (Ca(OH)₂ + 8 wt.% Cl⁻) was monitored before and after the testing, proving that the bulk pH did not vary during

C	Cr	Mn	Mo	N	Ni	P	S	Si
0.016	17.55	1.18	2.12	0.167	10.1	0.03	0.001	0.25

the testing. SSRT experiments were conducted with a strain rate of $1 \times 10^{-6} \text{ s}^{-1}$ to enable an increased number of environmental interactions⁷⁸. SSRT were under aerated conditions at room temperature (RT, 25 °C).

Electrochemical testing

Before the SCC testing, and without any applied stress, cyclic potentiodynamic polarization (CPP) tests were performed to better understand the corrosion performance of the corrugated (outermost surface influenced by the manufacturing process) and core sections (bulk of the sample, purely austenite matrix) at RT in aerated conditions. Samples were cut and isolated both ends to measure the influence of the manufacturing process, while epoxy mounted samples with the edges covered in epoxy lacquer were used to measure the core section. The potential scan ranged from $-300 \text{ mV}_{\text{OCP}}$ to $+1000 \text{ mV}_{\text{OCP}}$ at a potential scan rate of 1.667 mV s^{-1} , in accordance to ASTM G61-86⁷⁹. Three chloride concentrations were tested to the corrugated and core sections; 0, 4 and 8 wt.% of Cl⁻ by means of CaCl₂ additions to the concrete pore solution (pH 12.6) made out of a saturated Ca(OH)₂ following ASTM G1-03⁸⁰.

The electrochemical tests conducted during the straining of the sample were performed using a three-electrode configuration cell setup with a Gamry Reference 600 potentiostat. The reference electrode (RE) used in this test was a saturated calomel electrode (SCE), the counter electrode (CE) used was a graphite rod, and the working electrode (WE) was the AISI 316LN stainless steel reinforcement. All tests were performed in triplicate to ensure reproducibility.

The sequence for the different electrochemical test was the following: first open circuit potential (OCP) was monitored until a steady state OCP value was reached, and then electrochemical impedance spectroscopy (EIS) measurements were performed. The EIS measurements were recorded at the OCP, in a frequency range of $10^5 - 10^{-2} \text{ Hz}$ with an applied 10 mV AC excitation signal and at a step rate of 5 points per decade. This set of experiments was repeated with 3 h delay between each sequence, during these 3 h, a potentiostatic scan test monitored the current passing through the AISI 316LN stainless steel reinforcement with an applied potential (E_{app}) of $+200 \text{ mV}_{\text{SCE}}$. This E_{app} was kept constant throughout the entire loading.

Microstructure and fracture surface characterization

Microstructural analysis of AISI 316LN stainless steel reinforcement was conducted on cross-section area. The samples were epoxy

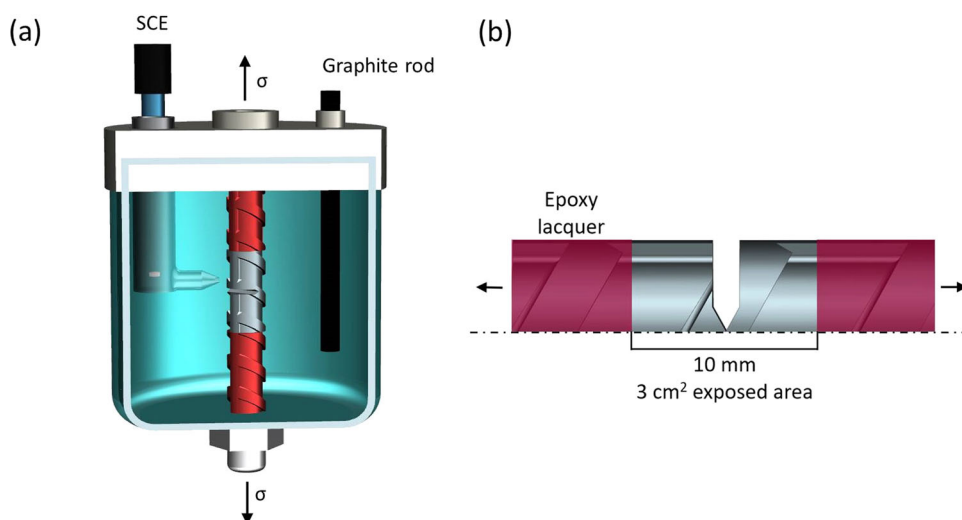


Fig. 8 Schematic representation of the SCC testing. (a) electrochemical cell, and (b) sketch of the notched AISI 316LN SS rebar.

mounted and polished to mirror finishing by SiC paper and diamond powder (1 μm). The etchant solution used to reveal the microstructure contained 30 ml HCl, 20 ml HNO₃, 10 ml deionized water and 3 ml H₂O₂, samples were exposed for 10 s⁸¹. The metallographic study was performed using scanning electron microscope SEM in a Tescan Lyra 3 XMU. The surface morphology of the broken samples was also studied by SEM. The SEM analysis was performed in secondary electron mode (SE) at an accelerating voltage of 15 kV and at a working distance of 10 mm. The Tescan Lyra 3 XMU SEM was also equipped with electron backscattered diffraction (EBSD), which was used to analyze the fraction of the phases and the crack path. The EBSD analysis was carried out at 10 kV accelerating voltage and at 0.5 μm in step size. Finally, X-ray diffraction (XRD) analysis was performed using a Rigaku SmartLab-3kW X-ray diffractometer, with a Cu target ($K_{\alpha} = 1.5406 \text{ \AA}$), and a scan step of 2 $^{\circ}$ /min over the 2θ range of 35 $^{\circ}$ –95 $^{\circ}$. The γ - and α' -phases were elucidated in the XRD patterns. Residual stresses were determined by XRD technique in the core and corrugate regions using the $\sin(2\psi)$ method. A voltage and current inputs of 40 kV and 40 mA were used for the Cu K_{α} radiation source⁸². The XRD system was calibrated with a stress-free sample, and the ASTM E915-96 was followed to check the X-ray alignment⁸³. The free residual stress peak for the XRD analysis was the austenitic (420) Bragg reflection found at $2\theta = 147^{\circ}$ ⁸⁴.

DATA AVAILABILITY

The data that support the findings of this study are available on request from the corresponding author upon reasonable request.

Received: 17 February 2023; Accepted: 23 October 2023;

Published online: 10 November 2023

REFERENCES

- McCafferty, E. *Introduction to corrosion science*, 1st edn. (Springer New York, 2010). <https://doi.org/10.1007/978-1-4419-0455-3>.
- Martin, U. & Bastidas, D. M. Stress corrosion cracking failure analysis of aisi 1018 carbon steel reinforcing bars in carbonated and chloride contaminated environment. *Eng. Fail. Anal.* **146**, 107159 (2023).
- Stress corrosion cracking in light water reactors: good practices and lessons learned* (International Atomic Energy Agency, 2011).
- Vermilyea, D. A. A theory for the propagation of stress corrosion cracks in metals. *J. Electrochem. Soc.* **119**, 405 (1972).
- Newman, R. C. & Healey, C. Stability, validity, and sensitivity to input parameters of the slip-dissolution model for stress-corrosion cracking. *Corros. Sci.* **49**, 4040–4050 (2007).
- Zhu, L. & Li, Y. Cleavage-dissolution assisted stress corrosion cracking under elastic loads. *npj Mater. Degrad.* **5**, 25 (2021).
- Katona, R. M. et al. Quantitative assessment of environmental phenomena on maximum pit size predictions in marine environments. *Electrochim. Acta* **370**, 137696 (2021).
- Ren, Z. & Ernst, F. Stress–corrosion cracking of AISI 316 L stainless steel in sea-water environments: Effect of surface machining. *Metals* **10**, 1324 (2020).
- Bastidas, D. M., Cobo, A., Otero, E. & González, J. A. Electrochemical rehabilitation methods for reinforced concrete structures: advantages and pitfalls. *Corros. Eng. Sci. Technol.* **43**, 248–255 (2008).
- Örnek, C. & Engelberg, D. L. Toward understanding the effects of strain and chloride deposition density on atmospheric chloride-induced stress corrosion cracking of type 304 austenitic stainless steel under MgCl₂ and FeCl₃:MgCl₂ droplets. *Corrosion* **75**, 167–182 (2019).
- Nakayama, G. & Sakakibara, Y. Prediction model for atmospheric stress corrosion cracking of stainless steel. *ECS Trans.* **52**, 303–311 (2013).
- Masuda, H. SKFM observation of SCC on SUS304 stainless steel. *Corros. Sci.* **49**, 120–129 (2007).
- Lynch, S. P. Mechanisms of hydrogen assisted cracking—a review. In *Hydrogen Effects on Material Behavior and Corrosion Deformation Interactions* (Eds. Moody, N. R., Thomson, A. W., Ricker R. E., Was, G. S. & Jones R. H.) 449–466. (Minerals, Metals & Materials Society, Warrendale, PA, 2003).
- Birnbaum, H. K. & Sofronis, P. Hydrogen-enhanced localized plasticity—a mechanism for hydrogen-related fracture. *Mater. Sci. Eng. A* **176**, 191–202 (1994).
- Robertson, I. M., Birnbaum, H. K. & Sofronis, P. Chapter 91 Hydrogen effects on plasticity. In *Dislocation in Solids* (eds. Hirth, J. P. & Kubin, L. B. T.-D. in S.) 15, 249–293 (Elsevier, 2009).
- Lynch, S. P. Mechanistic and fractographic aspects of stress-corrosion cracking (SCC). In *Stress Corrosion Cracking 3–89* (Elsevier, 2011). <https://doi.org/10.1533/9780857093769.1.3>.
- Wang, C. et al. Microstructure evolution and corrosion behavior of dissimilar 304/430 stainless steel welded joints. *J. Manuf. Process.* **50**, 183–191 (2020).
- Park, I., Kim, E.-Y. & Yang, W.-J. Microstructural investigation of stress corrosion cracking in cold-formed AISI 304 reactor. *Metals* **11**, 7 (2020).
- Newman, R. C., Sieradzki, K. & Isaacs, H. S. Stress-corrosion cracking of sensitized type 304 stainless steel in thiosulfate solutions. *Metall. Trans. A* **13**, 2015–2026 (1982).
- Moser, R. D., Singh, P. M., Kahn, L. F. & Kurtis, K. E. Chloride-induced corrosion resistance of high-strength stainless steels in simulated alkaline and carbonated concrete pore solutions. *Corros. Sci.* **57**, 241–253 (2012).
- Ghosh, S. & Kain, V. Effect of surface machining and cold working on the ambient temperature chloride stress corrosion cracking susceptibility of AISI 304 L stainless steel. *Mater. Sci. Eng. A* **527**, 679–683 (2010).
- Parkins, R. N. Stress corrosion cracking. *Metall. Rev.* **9**, 201–260 (1964).
- Alyousif, O. M. & Nishimura, R. On the stress corrosion cracking and hydrogen embrittlement behavior of austenitic stainless steels in boiling saturated magnesium chloride solutions. *Int. J. Corros.* **2012**, 1–11 (2012).
- Wang, Y., Wu, X. & Wu, W. Effect of α' martensite content induced by tensile plastic prestrain on hydrogen transport and hydrogen embrittlement of 304 L austenitic stainless steel. *Metals* **8**, 660 (2018).
- Katona, R. M., Carpenter, J., Schindelholz, E. J. & Kelly, R. G. Prediction of maximum pit sizes in elevated chloride concentrations and temperatures. *J. Electrochem. Soc.* **166**, C3364–C3375 (2019).
- Hurley, M. F. & Scully, J. R. Threshold chloride concentrations of selected corrosion-resistant rebar materials compared to carbon steel. *Corrosion* **62**, 892–904 (2006).
- Macdonald, D. D. The point defect model for the passive state. *J. Electrochem. Soc.* **139**, 3434–3449 (1992).
- Klapper, H. S., Zajec, B., Heyn, A. & Legat, A. Elucidating nucleation stages of transgranular stress corrosion cracking in austenitic stainless steel by in situ electrochemical and optical methods. *J. Electrochem. Soc.* **166**, C3326–C3335 (2019).
- Klapper, H. S. & Rebak, R. B. Assessing the pitting corrosion resistance of oilfield nickel alloys at elevated temperatures by electrochemical methods. *Corrosion* **73**, 666–673 (2017).
- Allain, S., Chateau, J.-P. & Bouaziz, O. A physical model of the twinning-induced plasticity effect in a high manganese austenitic steel. *Mater. Sci. Eng. A* **387–389**, 143–147 (2004).
- Martin, U., Röss, J. & Bastidas, D. M. Intergranular SCC mechanism of ultrasonic nanocrystalline surface modified AISI 304 SS in H₂SO₄ solution containing chloride. *Electrochim. Acta* **405**, 139622 (2022).
- Truschner, M. Effect of cold deformation on the stress corrosion cracking resistance of a high-strength stainless steel. *J. Mater. Sci.* **57**, 20447–20461 (2022).
- Kowaka, M. & Nagata, S. Stress corrosion cracking of mild and low alloy steels in CO-CO₂-H₂O environments. *Corrosion* **32**, 395–401 (1976).
- Katona, R. M., Karasz, E. K. & Schaller, R. F. A Review of the governing factors in pit-to-crack transitions of metallic structures. *Corrosion* **79**, 72–96 (2023).
- Martin, U., Röss, J., Bosch, J. & Bastidas, D. M. Stress corrosion cracking mechanism of AISI 316LN stainless steel rebars in chloride contaminated concrete pore solution using the slow strain rate technique. *Electrochim. Acta* **335**, 135565 (2020).
- Medina, E., Medina, J. M., Cobo, A. & Bastidas, D. M. Evaluation of mechanical and structural behavior of austenitic and duplex stainless steel reinforcements. *Constr. Build. Mater.* **78**, 1–7 (2015).
- Bautista, A., Alvarez, S. M., Paredes, E. C., Velasco, F. & Guzman, S. Corrugated stainless steels embedded in carbonated mortars with and without chlorides: 9-Year corrosion results. *Constr. Build. Mater.* **95**, 186–196 (2015).
- Marvasti, M. H. *Crack Growth Behavior of Pipeline Steels in Near Neutral pH Soil Environment*. Ph.D. thesis (University of Alberta, Canada, 2010).
- Galakhova, A., Prattes, K. & Mori, G. High-temperature high-pressure SCC testing of corrosion-resistant alloys. *Mater. Corros.* **72**, 1831–1842 (2021).
- Lin, S. & Hills, D. A. Stress intensity factors for cracks emanating from a semi-circular notch in a half-plate. *J. Strain Anal. Eng. Des.* **31**, 433–439 (1996).
- Li, T., Liu, L., Zhang, B., Li, Y. & Wang, F. Growth of single corrosion pit in sputtered nanocrystalline stainless steel film. *Corros. Sci.* **111**, 186–198 (2016).

42. Feng, X., Lu, X., Zuo, Y., Zhuang, N. & Chen, D. The effect of deformation on metastable pitting of 304 stainless steel in chloride contaminated concrete pore solution. *Corros. Sci.* **103**, 223–229 (2016).
43. Scully, J. C. The interaction of strain-rate and repassivation rate in stress corrosion crack propagation. *Corros. Sci.* **20**, 997–1016 (1980).
44. Macdonald, D. D. Passivity—the key to our metals-based civilization. *Pure Appl. Chem.* **71**, 951–978 (1999).
45. Diegle, R. B. & Boyd, W. K. The role of film rupture during slow strain rate stress corrosion cracking testing. In *Stress Corrosion Cracking: The Slow Strain-rate Technique* (eds. Ugiansky, G. M. & Payer, J. H.) 26–46 (ASTM International, 1979). <https://doi.org/10.1520/stp665-eb>.
46. Patel, J. R. & Cohen, M. Criterion for the action of applied stress in the martensitic transformation. *Acta Metall.* **1**, 531–538 (1953).
47. Hauser, M., Wendler, M., Weiß, A., Volkova, O. & Mola, J. On the critical driving force for deformation-induced α' -martensite formation in austenitic Cr–Mn–Ni steels. *Adv. Eng. Mater.* **21**, 1800676 (2019).
48. Bavay, J. C. Austenitic stainless steels. In *Stainless Steels* (eds. Lacombe, P., Baroux, B. & Beranger, G.) 551, (1993).
49. Hauser, M. et al. Thermodynamic-mechanical modeling of metastable high alloy austenitic CrMnNi steels. In *Austenitic Determination of residual stresses C. G.* 651–678 (Springer International Publishing, 2020). https://doi.org/10.1007/978-3-030-42603-3_20.
50. Ohta, K. & Ishida, H. Comparison among several numerical integration methods for Kramers-Kronig transformation. *Appl. Spectrosc.* **42**, 952–957 (1988).
51. Bastidas, D. M. Interpretation of impedance data for porous electrodes and diffusion processes. *Corrosion* **63**, 515–521 (2007).
52. Diaz, B., Guitián, B., Nóvoa, X. R. & Pérez, M. C. The effect of chlorides on the corrosion behaviour of weathered reinforcing bars. *Electrochim. Acta* **336**, 135737 (2020).
53. Hsu, C. H. & Mansfeld, F. Technical Note: concerning the conversion of the constant phase element parameter Y_0 into a capacitance. *Corrosion* **57**, 747–748 (2001).
54. Brug, G. J., van den Eeden, A. L. G., Sluyters-Rehbach, M. & Sluyters, J. H. The analysis of electrode impedances complicated by the presence of a constant phase element. *J. Electroanal. Chem. Interfacial Electrochem.* **176**, 275–295 (1984).
55. Naskar, A. et al. Pitting behavior of friction stir repair-welded 304 L stainless steel in 3.5% NaCl solution at room temperature: role of grain and defect structures. *SN Appl. Sci.* **2**, 2164 (2020).
56. Iuan-Jou Yang. Method for monitoring cracks and critical concentration by using phase angle. Patent 5,612,621 (1997).
57. Carmona-Hernandez, A. et al. Study of SCC of X70 steel immersed in simulated soil solution at different pH by EIS. *Materials* **14**, 7445 (2021).
58. Oskuie, A. A., Shahrabi, T., Shahriari, A. & Saebnoori, E. Electrochemical impedance spectroscopy analysis of X70 pipeline steel stress corrosion cracking in high pH carbonate solution. *Corros. Sci.* **61**, 111–122 (2012).
59. Lou, X. & Singh, P. M. Phase angle analysis for stress corrosion cracking of carbon steel in fuel-grade ethanol: experiments and simulation. *Electrochim. Acta* **56**, 1835–1847 (2011).
60. Ghobadi, M., Danaee, I., Saebnoori, E. & Eskandari, H. Impedance studies on stress corrosion cracking behavior of steel pipeline in NS4 solution under SSRT test condition. *Prot. Met. Phys. Chem. Surfaces* **57**, 634–646 (2021).
61. Bosch, R.-W. Electrochemical impedance spectroscopy for the detection of stress corrosion cracks in aqueous corrosion systems at ambient and high temperature. *Corros. Sci.* **47**, 125–143 (2005).
62. Martin Diaz, U., Birbilis, N., Macdonald, D. D. & Bastidas, D. M. Passivity breakdown and crack propagation mechanisms of lean duplex (UNS S32001) stainless steel reinforcement in high alkaline solution under stress corrosion cracking. *Corrosion* **79**, 4229 (2023).
63. Martin, U. & Bastidas, D. M. Stress corrosion cracking mechanisms of UNS S32205 duplex stainless steel in carbonated solution induced by chlorides. *Metals* **13**, 10645 (2023).
64. Li, B., Ren, F. C. & Tang, X. Y. The investigation on strain strengthening induced martensitic phase transformation of austenitic stainless steel: A fundamental research for the quality evaluation of strain strengthened pressure vessel. *IOP Conf. Ser. Earth Environ. Sci.* **128**, 012005 (2018).
65. Das, A., Chakraborti, P. C., Tarafder, S. & Bhadeshia, H. K. D. H. Analysis of deformation induced martensitic transformation in stainless steels. *Mater. Sci. Technol.* **27**, 366–370 (2011).
66. Streicher-Clarke, A., Speer, J., Matlock, D., Williamson, D. & DeCooman, B. Analysis of lattice parameter changes following deformation of a 0.19C-1.63Si-1.59Mn transformation-induced plasticity sheet steel. *Metall. Mater. Trans. A Phys. Metall. Mater. Sci.* **36**, 907–918 (2005).
67. Ahmed, I. I., da Fonseca, J. Q. & Sherry, A. H. Effects of martensite development on lattice strain evolution during the in situ deformation of austenitic stainless steels at cryogenic temperatures. *J. Strain Anal. Eng. Des.* **48**, 306–312 (2013).
68. Ladd, M. Looking at metal structures. In *Crystal Structures* (ed. Ladd, M. B. T.-C. S.) 92–114 (Elsevier, 1999). <https://doi.org/10.1533/9781782420460.92>.
69. Govindaraj, V. et al. Effect of manganese on the grain boundary network of lath martensite in precipitation hardenable stainless steels. *J. Alloys Compd.* **886**, 161333 (2021).
70. Birley, S. S. & Tromans, D. Stress corrosion cracking of 304 L austenitic steel and the martensite transformation. *Corrosion* **27**, 63–71 (1971).
71. Gussev, M. N. & Leonard, K. J. In situ SEM-EBSD analysis of plastic deformation mechanisms in neutron-irradiated austenitic steel. *J. Nucl. Mater.* **517**, 45–56 (2019).
72. Li, W., Gu, J., Deng, Y. & Li, J. Comprehending the coupled effect of multiple microstructure defects on the passive film features and pitting behavior of UNS S32101 in simulated seawater. *Electrochim. Acta* **411**, 140055 (2022).
73. Chang, L. et al. The effect of martensite on stress corrosion crack initiation of austenitic stainless steels in high-temperature hydrogenated water. *Corros. Sci.* **189**, 109600 (2021).
74. Karlsen, W., Diego, G. & Devrient, B. Localized deformation as a key precursor to initiation of intergranular stress corrosion cracking of austenitic stainless steels employed in nuclear power plants. *J. Nucl. Mater.* **406**, 138–151 (2010).
75. ISO 7539-6, Corrosion of metals and alloys - Stress corrosion testing - Part 6: Preparation and use of precracked specimens for tests under constant load or constant displacement, International Organization for Standardization, Geneva, Switzerland (2018).
76. Briz, E., Biezma, M. V. & Bastidas, D. M. Stress corrosion cracking of new 2001 lean-duplex stainless steel reinforcements in chloride contained concrete pore solution: An electrochemical study. *Constr. Build. Mater.* **192**, 1–8 (2018).
77. ASTM G129-21, Standard practice for slow strain rate testing to evaluate the susceptibility of metallic materials to environmentally assisted cracking, ASTM International, West Conshohocken, PA (2021). <https://doi.org/10.1520/G0129-21>.
78. Du, X. S. et al. Pre-strain enhances film rupture to promote SCC of brass in Mattsson's solution – a proposal for a film-rupture-induced SCC mechanism. *Corros. Sci.* **69**, 302–310 (2013).
79. ASTM G61-86(2018) Standard test method for conducting cyclic potentiodynamic polarization measurements for localized corrosion susceptibility of Iron-, Nickel-, or Cobalt-Based alloys, ASTM International, West Conshohocken, PA (2018). <https://doi.org/10.1520/G0061-86R18>.
80. ASTM G1-03(2017)e1 Standard practice for preparing, cleaning, and evaluating corrosion test specimens, ASTM International, West Conshohocken, PA (2017). <https://doi.org/10.1520/G0001-03R17E01>.
81. ASTM E407-07(2015)e1 Standard practice for microetching metals and alloys, ASTM International, West Conshohocken, PA (2015). <https://doi.org/10.1520/E0407-07R15E01>.
82. Cherif, A., Pyoun, Y. & Scholtes, B. Effects of ultrasonic nanocrystal surface modification (UNSM) on residual stress state and fatigue strength of AISI 304. *J. Mater. Eng. Perform.* **19**, 282–286 (2010).
83. ASTM E915-96, Standard test method for verifying the alignment of X-ray diffraction instrumentation for residual stress measurement, ASTM International, West Conshohocken, PA, (1996). <https://doi.org/10.1520/E0915-96>.
84. Fitzpatrick, M. E. et al. *Determination of residual stresses by X-ray diffraction – Issue 2, Measurement Good Practice Guide No. 52, National Physical Laboratory, UK* (2005).

ACKNOWLEDGEMENTS

This work has been supported by Firestone Research Grant 639430, and The University of Akron Fellowship FRC-207160 and FRC-207865. Authors wish to thank North American Stainless for providing stainless steel reinforcement. Moreover, the authors acknowledge the technical support and facilities from The National Center for Education and Research on Corrosion and Materials Performance (NCERCAMP-UA), The College of Engineering and Polymer Science, and The University of Akron.

AUTHOR CONTRIBUTIONS

U.M. conducted the experimental work under the supervision of D.M.B. U.M., N.B., D.D.M. and D.M.B. evaluated and visualized the results. U.M., N.B., D.D.M. and D.M.B. drafted, reviewed and edited the paper. D.M.B. provided funding support.

COMPETING INTERESTS

The authors declare no competing interests.

ADDITIONAL INFORMATION

Correspondence and requests for materials should be addressed to David M. Bastidas.

Reprints and permission information is available at <http://www.nature.com/reprints>

Publisher's note Springer Nature remains neutral with regard to jurisdictional claims in published maps and institutional affiliations.



Open Access This article is licensed under a Creative Commons Attribution 4.0 International License, which permits use, sharing, adaptation, distribution and reproduction in any medium or format, as long as you give appropriate credit to the original author(s) and the source, provide a link to the Creative Commons license, and indicate if changes were made. The images or other third party material in this article are included in the article's Creative Commons license, unless indicated otherwise in a credit line to the material. If material is not included in the article's Creative Commons license and your intended use is not permitted by statutory regulation or exceeds the permitted use, you will need to obtain permission directly from the copyright holder. To view a copy of this license, visit <http://creativecommons.org/licenses/by/4.0/>.

© The Author(s) 2023